

Conduction mechanisms and charge trapping control in SiO₂ nanoparticle MIM capacitors

Chenna R. Bheesayagari, Joan Pons-Nin, Albert Orpella, Bremnen Véliz,
Sandra Bermejo, Manuel Domínguez-Pumar

*Micro and Nano Technologies Group, Universitat Politècnica de Catalunya, Barcelona,
Spain.*

Abstract

The objective of this paper is to present a charge trapping control method for MIM capacitors in which the dielectric is made of electrospray-deposited silica nanoparticles. The influence of the bias voltage on the impedance spectra of the devices is analyzed, as well as the main conduction mechanisms along the structure. The control method allows to monitor and control the long term drifts in the impedance of these devices, which are a result of the applied bias voltages.

Keywords: MIM capacitors, Silica nanospheres, charge control, electrospray, sigma-delta control

1. Introduction

Metal-insulator-metal (MIM) capacitors are one of the essential components in analog, RF and mixed signal ICs due to their low parasitic capacitances and high conductive electrodes [1, 2]. Several studies have been made to improve the capacitance density and reduce the leakage current for SOC (system-on-chip) applications [3, 4, 5]. MIM capacitors are typically fabricated using photolithographic techniques with a continuous dielectric layer between the metal layers.

In recent years, though, dielectric nanoparticles, used as a dielectric material between metal electrodes, have been investigated to build enhanced capacitors with higher capacitance densities [6, 7, 8, 9]. In [10], it has been reported that a metal-insulator-metal structure with SiO₂ nanoparticles fabricated using an electrospray technique (eMIM capacitor or supercapacitor)

showed an increase of capacitance by a factor of 4.4 compared to that of a continuous dielectric layer. This reliable technique has the advantage of being carried out at room temperature [11, 12, 13] and not requiring high vacuum conditions. This allows the deposition of a wide ranging of nanomaterials on a wide variety of substrates, including for example carbon based devices [14, 15].

The typical electrosprayed eMIM capacitor consists of several layers of dielectric nanospheres sandwiched between two electrodes. When the eMIM based on silica nanoparticles is analyzed at low frequencies, the capacitance gets enhanced up to 1000 times [16], in comparison to the theoretical one with a continuous layer of the same dielectric, thickness and area.

This enhancement in capacitance is associated to charge accumulation on the surfaces of the nanospheres. It has also been noticed that increasing the number of layers of nanospheres, by reducing their diameter, results in a capacitance increase.

The recent advances in functional nanostructures along with their intrinsic advantage of large surface area to volume ratio has resulted in widespread use of supercapacitors as potential energy storage devices [17, 18]. Since the overall performance of the supercapacitor devices strongly depends on the properties and the structure of the component materials, characterization of different dielectric materials has become one of the most important aspects to be investigated to improve the energy storage performance.

The objective of this paper is twofold. First, to electrically characterize the devices, eMIMs made of silica nanoparticles, in DC and AC impedance for different bias voltages. It will be shown that the application of bias voltages generates fast changes in the impedance. At same time, if the bias voltage is maintained for long times, slow and small drifts, which can be associated to the presence of charge trapping in the nanospheres, can also be observed in the electrical characteristics. The second objective of the paper is to present a control method that allows to compensate and in real time these slow drifts. This way the main electrical characteristics of the devices can be conserved, even when bias voltages are applied to the devices for long times.

The paper is divided in 4 sections. Section 2 explains the device fabrication and characterization. Section 3 presents the small drifts with slow dynamics that can be appreciated when applying bias voltages. Finally, Section 4 shows the experimental results obtained with the controls.

2. Device Fabrication and Characterization

The eMIM capacitors used in this work have been fabricated at the UPC Clean Room facilities. A specific electrospray technique has been used to deposit the SiO_2 nanoparticles which constitute the dielectric layer. The fabrication process [10] starts with the deposition of a $17\text{ }\mu\text{m}$ thick photoresist layer on a glass substrate. A mask is then used to remove the photoresist in the active area. Next, a 427 nm -thick layer of aluminum is deposited by sputtering. Lift-off is then used to etch away the photoresist and, therefore, the bottom electrode is defined on the glass surface. An aqueous colloidal solution with 5% SiO_2 nanoparticles of 255 nm diameter is placed in a reservoir connected to a needle. A high voltage is then applied between the needle and the bottom electrode to generate an aerosol of tiny droplets containing the SiO_2 nanoparticles that are transported over to the bottom electrode. Finally, a second aluminum layer is deposited by thermal evaporation on top of the nanoparticles through a shadow mask. This layer, of $1.1\text{ }\mu$ thick, constitutes the top electrode.

A vertical cross section of the devices and a SEM capture showing the SiO_2 nanospheres constituting the dielectric are shown in Figure 1. The active area of the devices is 15.9 mm^2 . As commented above, nanoparticles contribute with a large amount of charge trapped at their interfaces that produces a strong increase of the capacitance of the device. Thus, the capacitance of the eMIMs fabricated is around $30\text{-}35\text{ nF}$, a value which is approximately 1000 times greater than that of a MIM with the same dimensions and a continuous silica layer as dielectric. Indeed, the eMIM can also be considered as a set of many RC sub-circuits connected in series, as shown in a recent work [16], but the values of the sub-capacitances are large enough that the total equivalent capacitance is still very high.

2.1. DC Characterization

A first objective of this work involves investigating the effects of the bias voltages applied on the electrical performance of the devices fabricated, in order to know which conduction mechanisms are dominant. The voltages applied can produce charge redistribution in the, nanosphere-based dielectric, which in turn can generate significant changes in the impedance spectra.

In order to know which conduction mechanisms dominate in experimental devices, I-V characterization curves are usually measured at different temperatures. By analyzing how the different conduction processes match the

experimental curves at different temperatures, it is possible to assign one or more specific conduction mechanisms to the devices. Poole-Frenkel (P-F) is a known conduction mechanism in dielectrics in which the thermal emission of trapped charges within the forbidden gap is enhanced by band tilting due to the application of an electric field. The probability of emission increases for increasing values of the electric field. The current density due to P-F emission is [19, 20]:

$$J = q\mu N_C E \exp \left[\frac{-q(\phi_T - \sqrt{qE/\pi\epsilon_r\epsilon_0})}{kT} \right], \quad (1)$$

where q is the electron charge, μ the electron drift mobility, N_C the density of states in the conduction band, E the electric field, ϕ_T the trap energy level, ϵ_r the optical dielectric constant, ϵ_0 the permittivity in vacuum, k the Boltzmann constant and T the temperature.

Figure 2 shows the measured I-V values (circles) and the modeled Poole-Frenkel (P-F) emission curves (solid lines) at different temperatures sweeping the range 30 °C - 60 °C. As it can be observed, the curves fit very well with the experimental data, indicating that P-F emission is the dominant conduction mechanism for this case. Figure 3(a) shows that $\ln(J/V)$ versus $V^{1/2}$ is linear for voltages above 0.5V, as is typical for P-F emission. The optical dielectric constant extracted from the fittings ranges from 2 for 30 °C to 1.7 for 60 °C, which corresponds to refractive indexes $n = \sqrt{\mu_r\epsilon_r}$ ranging from 1.4 to 1.3. These values fully match with those provided by the nanoparticle manufacturer [21].

The trap energy level obtained is constant at a value around 0.94 eV for all temperatures. The reduction of the current observed when the temperature rises is due to the evaporation of water molecules, which in turn produces a reduction of the electrical conduction associated with ions [16]. This effect produces a reduction of carrier drift mobility and also a small reduction of the dielectric constant as predicted by the P-F model.

For voltages below 0.5 V, the Ohmic conduction, due to small breaks in the dielectric layer, begins to gain influence, distorting the P-F curves of Figure 3(a). Figure 3(b) shows that the I-V curves for such low voltages tend to linear, as is typical when ohmic conduction dominates.

These results indicate that for low voltages the variation of current as a function of voltage, i.e. the changes in the impedance of the eMIM, is mainly

due to Ohmic conduction through possibly small breaks in the dielectric layer. For high voltages, P-F emission dominates the I-V dependence and, therefore, the variation of the impedance.

2.2. AC Characterization

The next step is to investigate the impedance spectra and how these are affected by the application of bias. To this end, an experiment has been performed in which different constant voltage stresses, ranging from -0.6 V to +0.6 V, are applied consecutively to the eMIM. For each voltage applied, the corresponding Nyquist plot was measured with a precision impedance analyser, using a 200 mV AC test signal and frequencies ranging from 20 Hz to 200 kHz. The Nyquist plots obtained are shown in Figure 4 (circles). A fast dynamics phenomenon, which produces noticeable changes in the impedance of the device when it is under different bias voltages, is clearly observed.

In order to obtain more information about the mechanisms that may be responsible for the observed behavior, fittings with a circuitual model have been made. Among the different models used, the transmission line equivalent model, derived from flux equations for two different mobile charge species [22, 23], gave the best results. This model provides a first representation for mixed ionic and electronic conduction (MIEC) devices. It is more physically oriented than other typical, and simpler, models such as Randles, where Warburg and constant elements are used [16, 24]. The parameters of the MIEC model, see Figure 5, are: 1) the distributed electron and ion resistances R_e and R_i (associated with conduction of these mobile charge species inside the dielectric), the distributed chemical capacitance C_{ch} (due to charge accumulated inside the dielectric), and the electronic and ionic capacitances and resistances of the electrodes R_{ke} , C_{ke} , R_{ki} , C_{ki} .

As can be observed in Table 1, R_i and R_e , which respectively model the behavior of electron and ion conduction, decrease as the bias voltage applied increases. This indicates that both carrier species increase conduction with bias voltage, mainly due to ohmic conduction at low voltages and due to P-F emission at high voltages. The variation is more noticeable in the ions case, therefore indicating that ions are more sensitive to voltage variation. On the other hand, the electron resistance, R_e , is several orders of magnitude lower than that of ions, R_i , as shown in Table 1, probably due to sluggish of the ion diffusion process [25] and therefore indicating that ion conduction velocity is much lower than that of electrons.

It can also be observed that the contact resistances R_{ke} and R_{ki} do not depend on the bias voltage, while the contact capacitance due to the accumulation of charge decreases with voltage variation only for ions (C_{ki}). This again suggests that ions are more sensitive to voltage changes. Moreover, we believe that the reduction of C_{ki} observed for high DC voltages may be due to thermal evaporation after contact heating.

On the other hand, the chemical capacitance, C_{ch} exhibits some small variation with the voltages applied, being its values around 0.3 nF. This chemical capacitance is associated with the amount of species (electrons and ions) accumulated into the device due to ambipolar diffusion mechanisms in terms of Fick's first law [23]. When DC voltage increases the diffusion coefficient also increases, producing a slight reduction of the chemical capacitance. Finally, the C_{ke} parameter is associated to electron accumulation near the contacts and it does not depend on diffusion mechanisms.

3. Towards the Control Method

Our next set of experiments is aimed at investigating the effect of applying voltages of different polarity for long times on a key feature of the device: its capacitance-voltage (C-V) characteristic. To this effect, the device was stressed with a sequence of alternative bias voltages of 0.6 V and -0.6 V in intervals of 2 hours, see Figure 6(a).

The C-V curves measured after each constant voltage application are shown in Figure 6(b). As it can be observed, the C-Vs have an approximately parabolic shape. It is also seen that horizontal C-V displacements to the right are produced at $t=2, 6, 10$ and 14 h, where the positive voltage was last applied. On the other hand, horizontal C-V displacements to the left are produced at $t=4, 8$ and 12 h, after the application of negative voltage. Accordingly with the discussions made in the previous section, two charge-related effects can be identified here: applying voltages of different sign produces noticeable effect in the Nyquist plot of the device, due to fast charge redistribution in the dielectric; whereas applying constant bias for a long time implies long term drifts in the impedance, due to charge trapping. This last effect is noticed by the horizontal shifts of the C-V characteristics.

The kind of behavior observed in the experiment of Figure 6 strongly resembles that obtained with MEMS switches working in open-state and MOS capacitors, [26]. For instance, having a parabolic C-V has been exploited for MEMS in [27, 28], where measuring the position of the C-V minimum

provides an estimation of the voltage shift produced by the amount of charge stored in the dielectric. However, this technique, referred to as center-shift method, is not compatible with obtaining the charging dynamics, because a certain time is required to perform each C-V measurement, which additionally will distort the amount of trapped charge, since different voltages are applied to obtain a single C-V curve. To solve this problem, a minimally invasive method, allowing to dynamically monitor the horizontal shifts of the C-V shifts, was proposed in [29, 30]. There, the voltage shift, and thus the charge status of the device, is obtained from only two capacitance values, measured at voltages of different sign in close instants of time, fast switching. All these methods are insensitive to vertical displacements of the C-V curve, an effect that is also observed in our experiments. These displacements are usually due to variation in environmental factors, such as temperature.

The opposite effects of applying voltages of different sign, together with the method of inferring the voltage C-V shift through two capacitance measurements are used in [29, 31] to implement a control strategy that allows controlling charge trapping. Concretely, a sigma-delta loop allows to successfully set and maintain the displacement of the C-V, and thus the voltage shift or the dielectric charge, to a target value.

Taking into account the parallelism of the results obtained with the MEMS case, we have used a similar control strategy to set and stabilize the C-V shift (and therefore the charging status) of our eMIM capacitors to a desired position. The first step towards this objective is to verify if the bipolar waveforms used for MEMS control in [29, 30] are also applicable to our case. These waveforms, called symbols BIT0 and BIT1 and described in Figure 7, allow both device actuation and C-V shift estimation. They have a total time length T_s and two voltage levels, $V^+ > 0$ and $V^- < 0$. In BIT0 (BIT1), $V^- (V^+)$ is applied for a time $(1 - \delta)T_s$, with $\delta < 1$, whereas $V^+ (V^-)$ is applied for a shorter time δT_s .

The parameters V^- , V^+ , δ and T_s are chosen so that applying BIT0 or BIT1 generates horizontal C-V shifts of different sign. Moreover, accordingly to the experimental results reported above, in Figure 6(b), applying BIT0s to our eMIM capacitors should produce left shifts of the C-V; and, symmetrically, BIT1s should produce right shifts of the C-V. Figure 7 also illustrates the desired effect of BIT0 and BIT1 on the C-V shifts.

Additionally, a differential capacitance ΔC is obtained from two capaci-

tance measurements performed within each symbol, as follows:

$$\Delta C = C(V^+) - C(V^-) = \begin{cases} C(T_s) - C((1 - \delta)T_s), & \text{BIT0} \\ C((1 - \delta)T_s) - C(T_s), & \text{BIT1} \end{cases} \quad (2)$$

On the other hand, the parabolic function used to model the C-V characteristic of our devices can be written as:

$$C(V, t) = \alpha(V - V_{sh}(t))^2 + C_0, \quad (3)$$

where V_{sh} is the voltage shift, α is the parabola parameter and C_0 is the minimum value of the capacitance. These two parameters can be easily obtained by fitting (3) with the measurement data.

As it is well known, small changes in temperature or humidity could result in vertical displacements of the C-V. These influences can be accounted as slow time variations $C_0(t)$. Just to minimize these effects, at the end of each symbol the capacitance measurements are taken at two different points of the C-V curve in close instants of time t and $t + \Delta t$ such that Δt is smaller than the time constants involved in the dynamics of the device. In such a case, we can write $C_0(t) = C_0(t + \Delta t)$. With this approach the differential capacitance obtained at the end of each symbol can be written as:

$$\Delta C = \alpha[(V^+)^2 - (V^-)^2] - 2\alpha V_{sh}[V^+ - V^-], \quad (4)$$

which illustrates the relation between the voltage shift and the quasi-differential capacitance. It also indicates that ΔC is independent of $C_0(t)$, and therefore it is not sensitive to the vertical shifts of the C-V that may occur during the measurements.

As commented above, the main objective of the control is to maintain a desired state variable by periodically monitoring it and applying an appropriate sequence of control signals through a feedback loop. In this case of eMIM capacitors, the state variable to be monitored and controlled is the differential capacitance ΔC . Figure 7 also illustrates the control strategy: a value of ΔC (then of V_{sh} , or of the charge status in the dielectric) is measured at the end of each BITx application. Comparing this value with a previously given threshold ΔC_{th} , the next symbol to be applied, either a BIT0 or a

BIT1, is decided according to the following law:

$$\text{next } BIT = \begin{cases} BIT1 & \text{when } \Delta C < \Delta C_{th}, \\ BIT0 & \text{otherwise,} \end{cases} \quad (5)$$

Now the implementation of the control using sigma-delta modulation becomes straightforward, as shown in Figure 8. The control circuit samples ΔC at periodic times nT_s , and uses a first-order sigma-delta loop to apply an adequate sequence of bipolar symbols BIT0 and BIT1 during the next sampling intervals to maintain it around a previously given threshold value ΔC_{th} .

4. Experimental Results and Discussion

The experiments reported in this section have two main objectives. The first is to observe the drift dynamics in the device through open loop experiments and to verify that the application of symbols BIT0 and BIT1 produces the expected effects in the form of C-V shifts in opposite directions.

The second objective is to investigate the effectiveness of the proposed control. In particular, that it allows the continuous compensation of this drift, therefore entailing stabilization of the impedance of the device in the long term. Possible applications of this type of controls are reliability and lifetime improvement or performance improvement in sensing applications.

4.1. Open loop Experiments

The charging dynamics can be seen in Figure 9, which shows the evolution of $\Delta C(t)$ for the continuous application of BIT0 and BIT1 waveforms, in time intervals of 4h. As it can be observed, BIT1s tend to decrease $\Delta C(t)$, therefore increasing the associated voltage shift, whereas the opposite behaviour can be noticed with the application of BIT0 waveforms. These results are consistent with those in Figure 6, where the continuous application of 0.6 V increased the voltage shift (and the reverse behaviour was obtained for -0.6 V).

Now, Figure 10 shows the Nyquist plots of the same experiment, measured every 4 h. After each period of 4h, three Nyquist plots are measured at: 0 V, 40 mV and 70 mV. The bottom plot shows a zoom of the final part of the Nyquist plots. The order to the initial plot is (70 mV \rightarrow 40 mV \rightarrow 0 V). The application of BIT1s tends to impose this order in the Nyquist plot: (70 mV

$\rightarrow 40 \text{ mV} \rightarrow 0 \text{ V}$). The application of BIT0s tends to impose either ($40 \text{ mV} \rightarrow 0 \text{ V} \rightarrow 70 \text{ mV}$) or ($0 \text{ V} \rightarrow 40 \text{ mV} \rightarrow 70 \text{ mV}$). This means that applying BIT0s (which is equivalent to apply a negative voltage most of the time) tends to decrease the Nyquist plot for 0 V , whereas the opposite behaviour is obtained for BIT1.

Discussion. From these open loop experiments, it is obvious that BIT0 and BIT1 waveforms are effective in generating voltage shifts of different sign. These voltage shifts can be understood as small shifts of the Nyquist plots taken at any bias voltage. In our case, since the observed shifts in the C-V curves are small ($< 100 \text{ mV}$), the effect can be seen more easily when the Nyquist plots are taken with low bias voltages (voltages of the order of the shifts in the C-V curves). In our case, then, the Nyquist plots at 0 V , 40 mV and 70 mV are reordered.

4.2. Closed loop Experiments

In these experiments the control method proposed has been applied to our eMIM capacitors. To minimize the effects of environmental variations in the capacitance measurements, the device has been maintained at a constant temperature on a thermal chuck using a STC200 temperature controller. A precision LCR Meter has been used to generate the BIT waveforms and to perform the periodic capacitance measurements. C-V measurements with a $500 \text{ mV}@100 \text{ KHz}$ AC test signal have also been performed.

The first experiment reported was aimed at investigating the control capabilities. It consisted of applying the control to reach a sequence of seven different values of ΔC_{th} , ranging from -60 to 120 pF and each lasting for 15 min . At the end of each ΔC_{th} step, the control was paused to perform a fast C-V measurement. A constant temperature of $50 \text{ }^\circ\text{C}$ is maintained to minimize the vertical displacements in the C-V curves. Figure 11 shows the evolution of the differential capacitance ΔC as a function of time. A transient can be observed at the beginning of each interval where ΔC either increases or decreases with the application of BIT0/BIT1 waveforms until it reaches the desired threshold ΔC_{th} . Once this target has been reached, the control loop injects appropriate BIT sequences to keep it constant. The "noisy" shape of the curve is due to the voltage switching made at each BIT, necessary to measure ΔC . Let us note that, although the control experiments performed have not been very long (105 min in the experiment reported in Figure 11 and 14 h in that reported later in Figure 13, no specific reliability problems that might be linked to the fast switching produced by the control

have been observed. On the other hand, let us also note that the thermal effects have been negligible in our control experiments, since the maximum power dissipated is approximately $0.1 \mu\text{W}$ (the applied voltages are $\pm 0.6 \text{ V}$ and the real part of the impedance is above $3.5 \text{ M}\Omega$).

The evolution of the average bitstream provided by the control loop is also shown in Figure 11. It is observed that each time a new target is set, the feedback loop applies a continuous sequence of BIT0/BIT1 waveforms until it reaches such target; after that a slow evolution of the average bitstream is always observed. However, the threshold level set at $t=90 \text{ min}$, $\Delta C_{th}=120 \text{ pF}$, is so large that the control loop could not reach it in the short time lapse considered. Additionally, Figure 12 shows the displacements of the C-V characteristics of the device obtained at the end of each control experiment. The corresponding voltage shift values measured taking 0 V as the initial voltage shift are also shown.

We can conclude that, within some limits, the experiment demonstrates that the control proposed allows successfully setting and stabilizing the shift of the C-V to previously given target positions. Moreover, in each control step the behaviour observed strongly resembles that of a sliding mode controller [32, 33]: an initial transient-reaching phase, with fast dynamics and strong variation of the bitstream, until the threshold value is reached; then, a steady-state sliding phase, in which slow dynamics and thus slow variation of the bitstream is observed. This behavior has also been reported and analyzed in other works, in which sigma-delta loops are used to control other types of devices, such as wind anemometers, MEMS switches or MOS capacitors [32, 33].

Finally, a long-time control experiment has been scheduled, with several different values of ΔC_{th} , now each lasting for 2 hours. The temperature was set to $50 \text{ }^\circ\text{C}$ and fast C-V measurements were performed at the end of the control steps. The evolution of ΔC and the bitstream during the experiment are plotted in Figure 13. It can be seen that all targets are reached successfully. Besides, as it was also observed in the previous control experiment, at each control step the sigma-delta loop applies either a BIT0 or a BIT1 waveform during the initial transient (reaching phase), and that once it reaches the threshold level it injects an appropriate sequence of BIT0-BIT1 waveforms to maintain ΔC almost constant around ΔC_{th} (sliding phase). The slow evolution of the average bitstream in the sliding phase, here more noticeable than in the experiment of Figure 11, gives the BIT0/BIT1 ratios (and thus the average voltage) necessary to maintain the control during the

experiment. Figure 14 shows the horizontal displacements of the C-V characteristics of the device and the voltage shift values measured at the end of each control step.

Conclusions

Electrical characterization to investigate the dominant conduction mechanisms in MIM capacitors with electrospray-deposited SiO_2 nanoparticles as dielectric has been performed. Poole-Frenkel emission has been identified as the main conduction mechanism for high bias voltages applied, whereas ohmic conduction becomes dominant for low voltages. It has been also found that the constant application of a bias voltage generates drifts in the impedance of the device and presents a double dynamics: a fast one in which the Nyquist plot changes instantaneously and a second one, in which the application of the bias for long times generates small drifts.

It has been demonstrated that it is possible to control successfully the drift of the C-V characteristic of the capacitors by generating an appropriate average bias voltage, using a control based on sigma-delta modulation. This entails the possibility of stabilizing the impedance of this kind of devices at long term, with potential benefits such as reliability improvements or performance improvements in sensing applications.

Acknowledgements

This work was supported by the Spanish Ministry MINECO under project RTI2018-098728-B-C33, by the European Space Agency under project ESA AO/1-8876/17/NL/CRS and by SENESCYT of the republic of Ecuador under agreement 2016-AR5G8871.

References

- [1] J. Babcock, S. Balster, A. Pinto, C. Dirnecker, P. Steinmann, R. Jumpertz, B. El-Kareh, Analog characteristics of metal-insulator-metal capacitors using PECVD nitride dielectrics, *IEEE Electron Device Letters* 22 (5) (2001) 230–232. doi:10.1109/55.919238.
- [2] H. Kwon, I. Han, S. Park, J. Bok, Y. Jung et al., Conduction mechanism and reliability characteristics of a metal–insulator–metal capacitor with

- single ZrO₂ layer, Japanese Journal of Applied Physics 50 (4S) (2011) 04DD02. doi:10.1143/JJAP.50.04DD02.
- [3] N. Inoue, I. Kume, J. Kawahara, S. Saito, N. Furutake, T. Toda et al., Surface control of bottom electrode in ultra-thin SiN metal–insulator–metal decoupling capacitors for high speed processors, Japanese journal of Applied Physics 46 (4S) (2007) 1968. doi:10.1143/JJAP.46.1968.
 - [4] T. Ono, K. Kato, H. Toyota, Y. Fukuda, Y. Jin, Characterization of metal–insulator–metal electrical properties of electron cyclotron resonance plasma deposited Ta₂O₅, Japanese journal of Applied Physics 45 (9S) (2006) 7345. doi:10.1143/JJAP.45.7345.
 - [5] S. Park, C. Park, D. Gilmer, H. Park, C. Kang, K. Lim, C. Burham, J. Barnett, P. Kirsch, H. Tseng et al., Bulk and interface effects on voltage linearity of ZrO₂–SiO₂ multilayered metal-insulator-metal capacitors for analog mixed-signal applications, Applied Physics Letters 95 (2) (2009) 022905. doi:10.1063/1.3182856.
 - [6] G. Topasna, Capacitance of spherical dielectric layers, Journal of Applied Physics 100 (2) (2006) 024501. doi:10.1063/1.2211302.
 - [7] K. Leonard, W. Suyama, M. Anderson, Evaluating the electrochemical capacitance of surface-charged nanoparticle oxide coatings, Langmuir 28 (15) (2012) 6476–6484. doi:10.1021/la204173w.
 - [8] K. Leonard, W. Suyama, M. Anderson, Improvement of electrochemical capacitor electrodes using SiO₂ nanoparticles, Electrochimica Acta 56 (27) (2011) 10137–10144. doi:10.1016/j.electacta.2011.08.116.
 - [9] Y. Cheng, Z. Wei, Q. Du, F. Liu, X. Duan, Y. Wang, D. Jia, Y. Zhou, B. Li, The shape effect of manganese(ii,iii) oxide nanoparticles on the performance of electrochemical capacitors, Electrochimica Acta 284 (2018) 408–417. doi:10.1016/j.electacta.2018.07.177.
 - [10] B. Véliz, S. Bermejo, A. Coll, L. Castañer, Metal–insulator–metal capacitor using electrosprayed nanoparticles, Applied Physics Letters 105 (1) (2014) 013109. doi:10.1063/1.4889746.

- [11] A. Coll, S. Bermejo, L. Castañer, Self-assembly of ordered silica nanostructures by electrospray, *Microelectronic Engineering* 121 (2014) 68–71. doi:10.1016/j.mee.2014.03.031.
- [12] L. Castañer, S. Bermejo, M. Dominguez-Pumar, Effect of dielectrophoretic force in the self-assembly process of electrosprayed nanoparticles, *Journal of Electrostatics* 87 (2017) 257–262. doi:10.1016/j.elstat.2017.05.007.
- [13] B. Véliz, S. Bermejo, J. Vives, L. Castañer, Large area deposition of ordered nanoparticle layers by electrospray, *Colloid and Interface Science Communications* 25 (2018) 16–21. doi:10.1016/j.colcom.2018.06.001.
- [14] A. Varea, O. Monereo, E. Xuriguera, J. Prades, A. Cirera, Electrospray as a suitable technique for manufacturing carbon-based devices, *Journal of Physics D: Applied Physics* 50 (2017) 1–10. doi:10.1088/1361-6463/aa798b.
- [15] J. Yan, Y. Leng, Y. Guo, G. Wang, P. G. H. Gong, P. Tan, Y. Long, X. Liu, W. Han, Highly conductive graphene paper with vertically aligned reduced graphene oxide sheets fabricated by improved electrospray deposition technique, *ACS Applied Materials and Interfaces* 11 (2019) 10810–10817. doi:10.1021/acsami.8b19811.
- [16] B. Véliz, S. Bermejo, A. Orpella, L. Castañer, Impedance modeling of silica nanoparticle metal-insulator-metal capacitors, *Electrochimica Acta* 280 (2018) 62–70. doi:10.1016/j.electacta.2018.05.084.
- [17] S. Sedira, B. Mendaci, Hydrothermal synthesis of spherical carbon nanoparticles (CNPs) for supercapacitor electrodes uses, *Materials for Renewable and Sustainable Energy* 9 (2019) 1–9. doi:10.1007/s40243-019-0161-0.
- [18] G. Tan, F. Wu, C. Zhan, J. Wang, D. Mu, J. Lu, K. Amine, Solid-state li-ion batteries using fast, stable, glassy nanocomposite electrolytes for good safety and long cycle-life, *NanoLetters* 16 (2016) 1960–1968. doi:10.1021/acs.nanolett.5b05234.
- [19] F. Chiu, A review on conduction mechanisms in dielectric films, *Advances in Materials Science and Engineering* (2014) 1687–8434doi:10.1155/2014/578168.

- [20] S. Sze, K. Ng, Physics of Semiconductor Devices. Third Edition, Wiley, NJ, USA, 2006.
- [21] Research and technology oriented microParticles GmbH, <http://microparticles.de/en/properties.html>, Last accessed on 2020-02-26.
- [22] J. Jamnik, J. Maier, Treatment of the impedance of mixed conductors. Equivalent circuit model and explicit approximate solutions, Journal of the Electrochemical Society 146 (11) (1999) 4183–4188. doi:10.1149/1.1392611.
- [23] W. Lai, S. Haile, Impedance spectroscopy as a tool for chemical and electrochemical analysis of mixed conductors: A case study of ceria, Journal of the American Ceramic Society 88 (11) 2979–2997. doi:10.1111/j.1551-2916.2005.00740.x.
- [24] B. Véliz, A. Orpella, S. Bermejo, Capacitance study of a polystyrene nanoparticle capacitor using impedance spectroscopy, Nanotechnology 30 (40) (2019). doi:10.1088/1361-6528/ab2d58.
- [25] G. Gregori, R. Merkle, J. Maier, Ion conduction and redistribution at grain boundaries in oxide systems, Progress in Materials Science 89 (2017) 252–305. doi:10.1016/j.pmatsci.2017.04.009.
- [26] M. Dominguez-Pumar, C. Bheesayagari, S. Gorreta, G. Lopez, I. Martin, E. Blokhina, J. Pons-Nin, Charge trapping control in MOS capacitors, IEEE Trans. Ind. Electron. 64–4 (2017) 3023–3029. doi:10.1109/TIE.2016.2645159.
- [27] R. Herfst, H. Huizing, P. Steeneken, J. Schmitz, Characterization of dielectric charging in RF MEMS capacitive switches, in: 2006 IEEE Int. Conf. on Microelectronic Test Structures, 2006, pp. 133–136. doi:10.1109/ICMTS.2006.1614290.
- [28] R. Herfst, P. Steeneken, H. Huizing, J. Schmitz, Center-shift method for the characterization of dielectric charging in RF MEMS capacitive switches, IEEE Trans. on semiconductor manufacturing 21 (2) (2008) 148–153. doi:10.1109/TSM.2008.2000285.

- [29] S. Gorreta, J. Pons-Nin, E. Blokhina, O. Feely, M. Dominguez-Pumar, Delta-Sigma Control of Dielectric Charge for Contactless Capacitive MEMS, *IEEE J. of Microelectromech. Syst.* 23 (4) (2014) 829–841. doi:10.1109/JMEMS.2013.2295842.
- [30] M. Dominguez-Pumar, S. Gorreta, J. Pons-Nin, E. Blokhina, P. Giounanlis, O. Feely, Real-Time Characterization of Dielectric Charging in Contactless Capacitive MEMS, *Analog Integrated Circuits and Signal Processing* 82 (3) (2015) 559–569. doi:10.1007/s10470-014-0458-y.
- [31] S. Gorreta, J. Pons-Nin, E. Blokhina, M. Dominguez-Pumar, A second-order delta-sigma control of dielectric charge for contactless capacitive MEMS, *IEEE J. of Microelectromech. Syst.* 24 (2) (2015) 259–261. doi:10.1109/JMEMS.2015.2402394.
- [32] M. Dominguez-Pumar, S. Gorreta, J. Pons-Nin, Sliding Mode Analysis of the Dynamics of Sigma-Delta Controls of Dielectric Charging, *IEEE Trans. Ind. Electron.* 63 (4) (2016) 2320–2329. doi:10.1109/TIE.2015.2509914.
- [33] M. Dominguez-Pumar, S. Gorreta, M. Atienza, E. Blokhina, J. Pons-Nin, Sliding mode control of heterogeneous systems, in: *Extended Abstracts Spring 2016*, Springer Int. Publishing, 2017, pp. 49–53. doi:10.1007/978-3-319-55642-0.

Tables and Figures

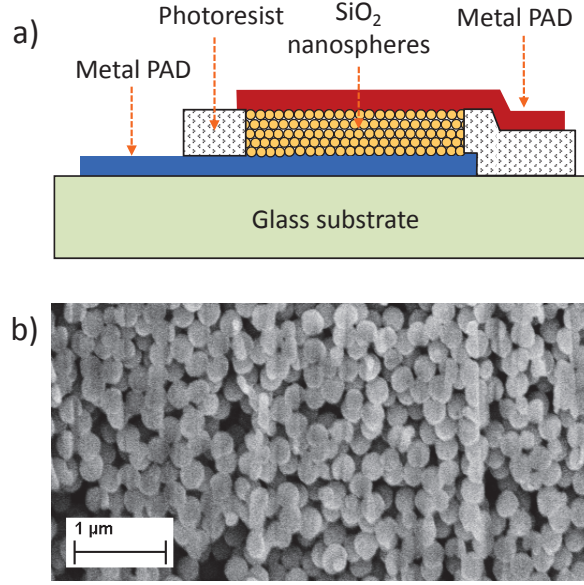


Figure 1: a) Schematic cross section of the devices fabricated. b) SEM capture of the dielectric layer.

Table 1: Fitting parameters of the MIEC model in Figure 4.

Bias [V]	0.05	0	-0.05	0.3	-0.3	0.6	-0.6
R_e [Ω]	140	110	140	110	80	70	70
R_i [$M\Omega$]	10.5	10.1	9.7	7.4	4.65	1.5	1.2
R_{ke} [$M\Omega$]	300	300	300	300	300	350	350
R_{ki} [$M\Omega$]	2.1	2.1	2.1	2.1	2.1	1.95	1.21
C_{ke} [pF]	450	450	450	450	450	480	480
C_{ki} [pF]	1000	1000	1000	800	550	200	200
C_{ch} [pF]	380	396	412	243	391	267	333

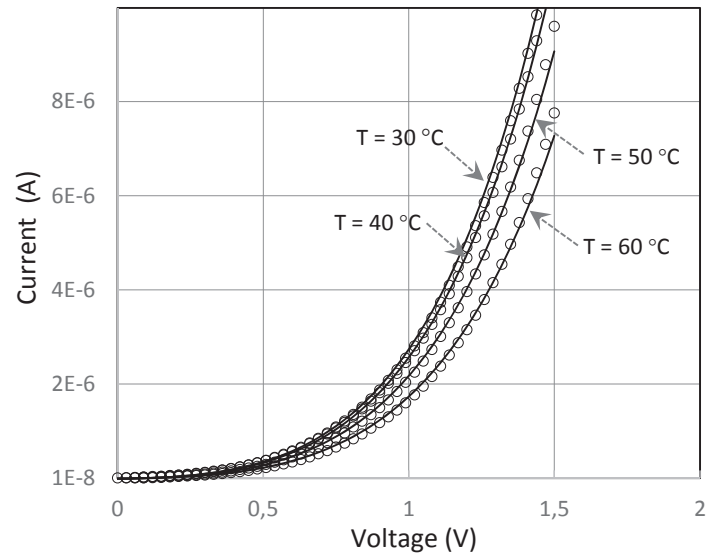


Figure 2: Experimental I-V curves of the eMIM (circles) and fitting curves of P-F emission (solid lines) for different temperatures.

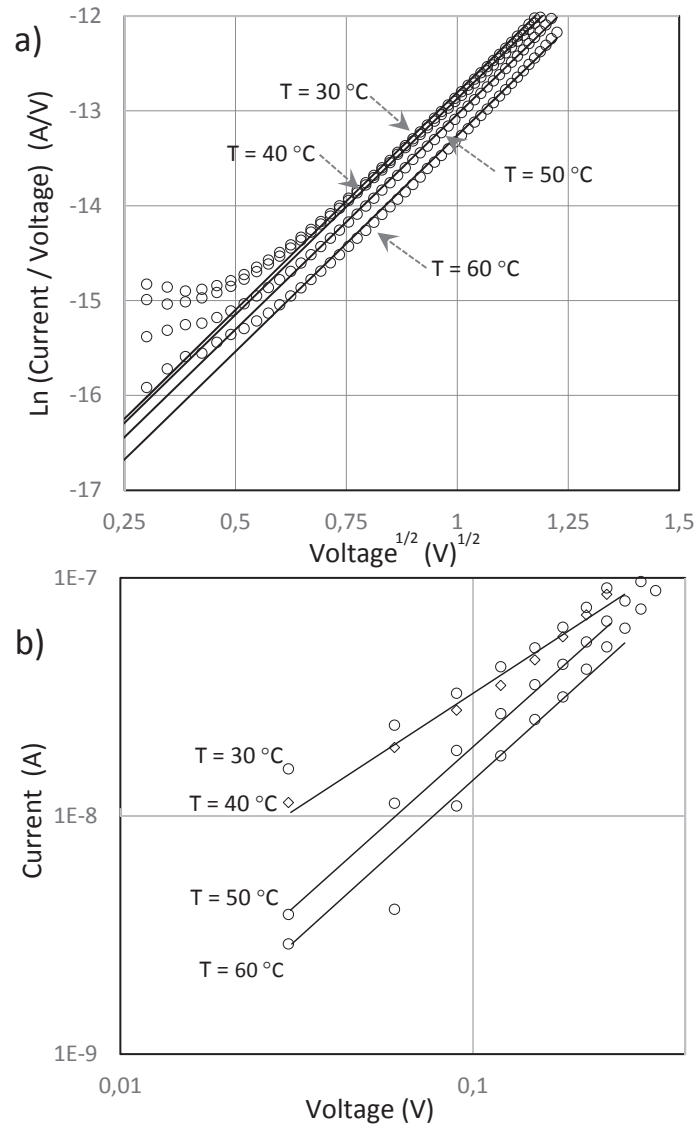


Figure 3: a) Characteristics of P-F emission at various temperatures for high voltages. b) Characteristics of Ohmic conduction at various temperatures for low voltages. Experimental values are represented as circles, whereas solid lines correspond to model fittings.

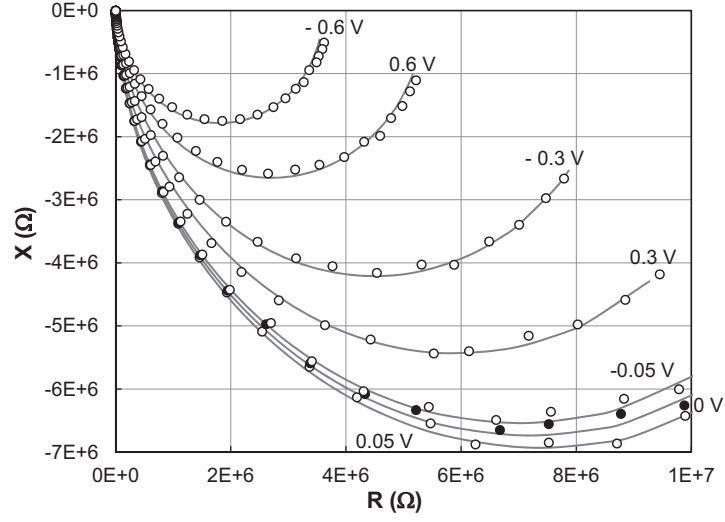


Figure 4: Circles: Nyquist plots measured when different constant voltages are applied successively to the eMIM capacitor. The continuous plots are fittings of the experimental results using the MIEC model of Figure 5.

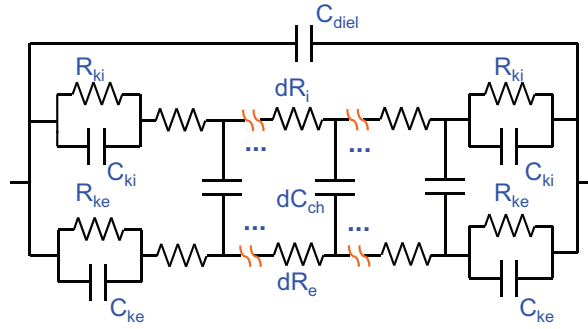


Figure 5: Mixed ionic and electronic conduction circuitual model, which contemplates effects associated to two different mobile charge species.

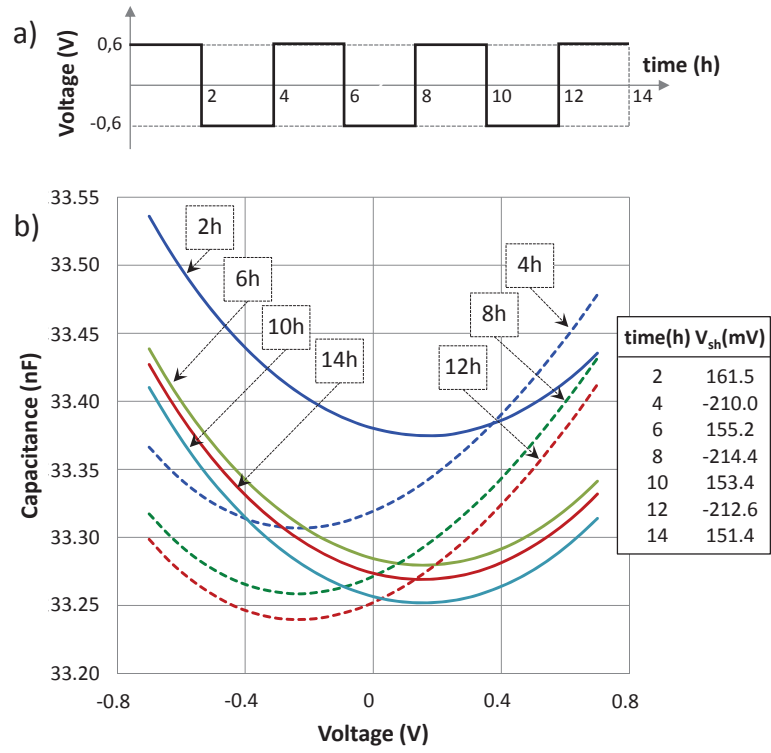


Figure 6: 14-hour experiment in which a sequence of bias voltages was applied to the device in 2 h intervals. Plot a) shows the sequence of voltages applied, plot b) the C-V curves measured at the end of each 2 h period at constant voltage. Dotted lines correspond to C-Vs measured after applying -0.6 V, and continuous lines after applying 0.6 V. The table indicates the position of the bottom of the C-V (voltage shift, V_{sh}) after each bias voltage application.

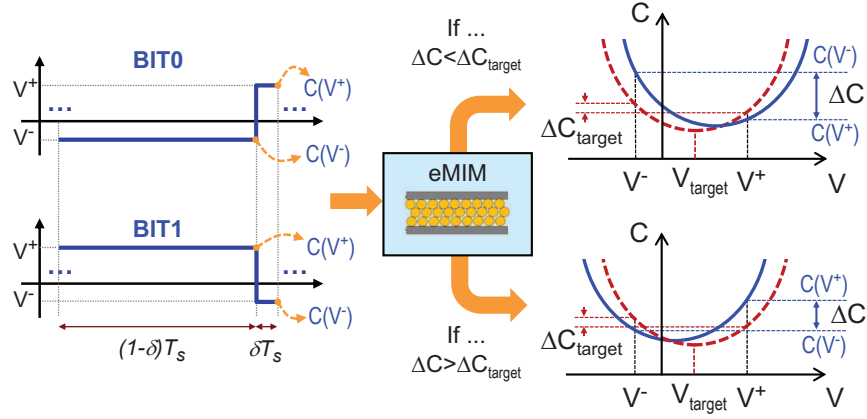


Figure 7: BIT1 and BIT0 actuation and sensing waveforms. Application of BIT1 (BIT0) waveforms tends to increase (decrease) the voltage shift of the C-V characteristic of the device [31].

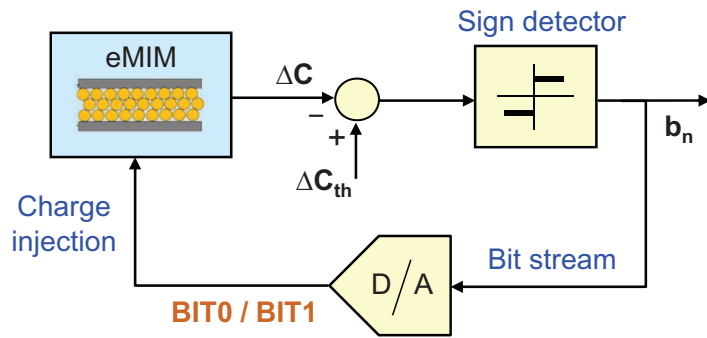


Figure 8: Sigma-Delta control architecture applied to the eMIM capacitors.

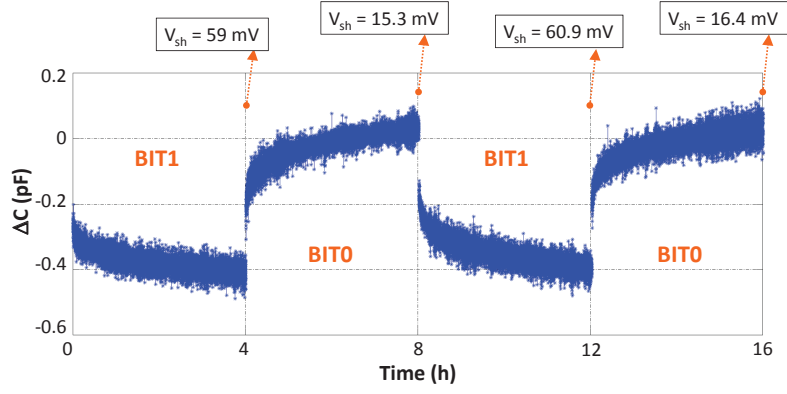


Figure 9: Evolution of $\Delta C(t)$ for an experiment in which BIT1 and BIT0 symbols were alternated in intervals of 4h each. BIT parameters: $V^+=0.6$ V, $V^-=-0.6$ V, $T_s=900$ ms, $\delta=1/4$. Capacitance is measured at 10 KHz. The values of the voltage shift calculated at the end of each BITx stress are also described.

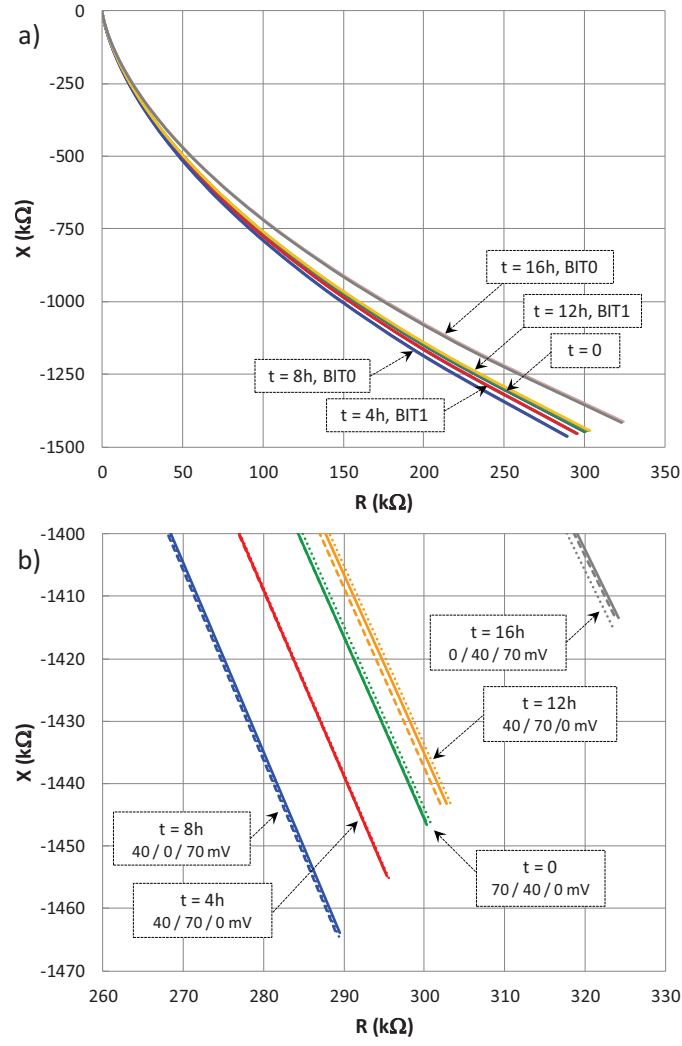


Figure 10: Groups of Nyquist plots at bias voltages: 0 V, 40 mV and 70 mV after each step of the experiment reported in Figure 9. Each group of three Nyquist plots is measured at time intervals of 4 h. The bottom graph is a zoom of the Nyquist plots. The Nyquist plots change their order depending on the history of the actuation waveform applied.

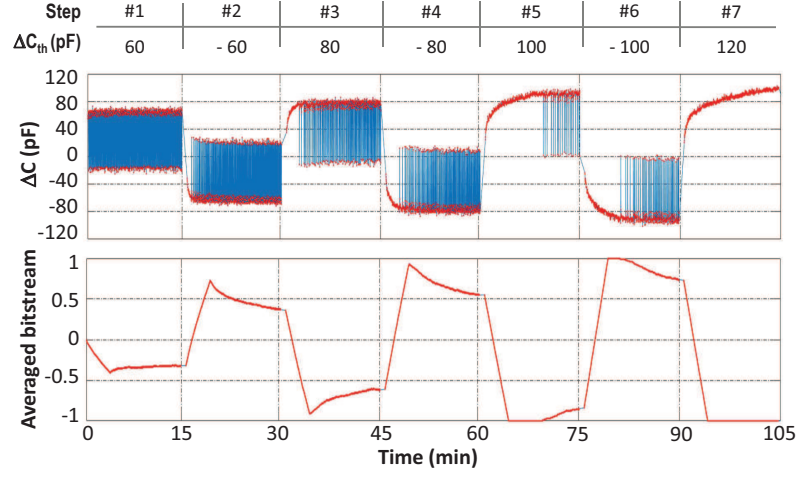


Figure 11: Experiment in which the sequence of threshold values listed above was applied. BITx parameters: $V^+=0.6$ V, $V^-=-0.6$ V, $T_s=1$ s and $\delta=1/5$. Top plot: Evolution of the differential capacitance, ΔC measured during the experiment. Bottom plot: Evolution of the average bitstream.

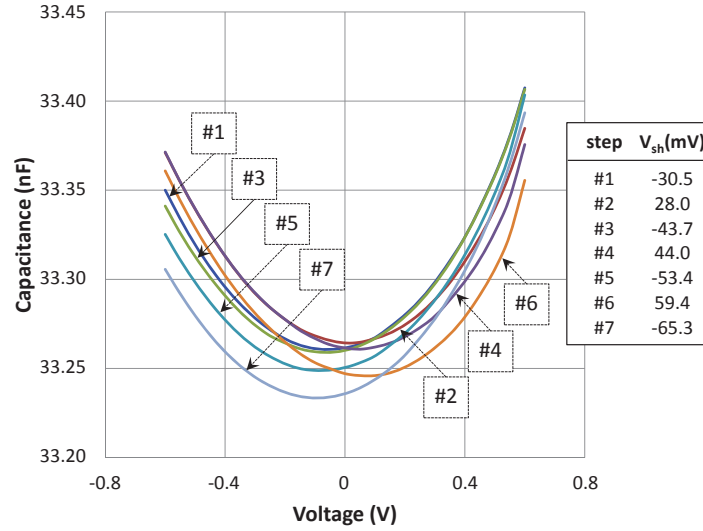


Figure 12: C-V characteristics measured at the end of each control step in the experiment of Figure 11. The table indicates the voltage shifts obtained after each step.

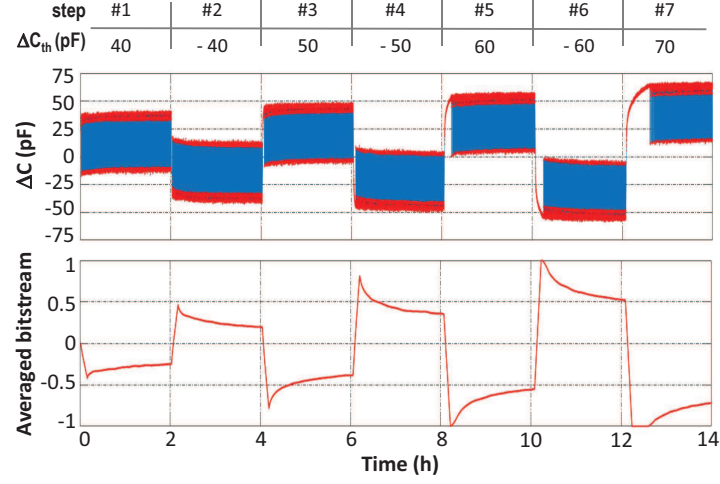


Figure 13: Experiment in which the sequence of threshold values listed above was applied. Parameters: $V^+ = 0.6$ V, $V^- = -0.6$ V, $T_s = 1$ s and $\delta = 1/5$. Top plot: Time evolution of the differential capacitance, ΔC . Bottom plot: Evolution of the average bitstream during the experiment.

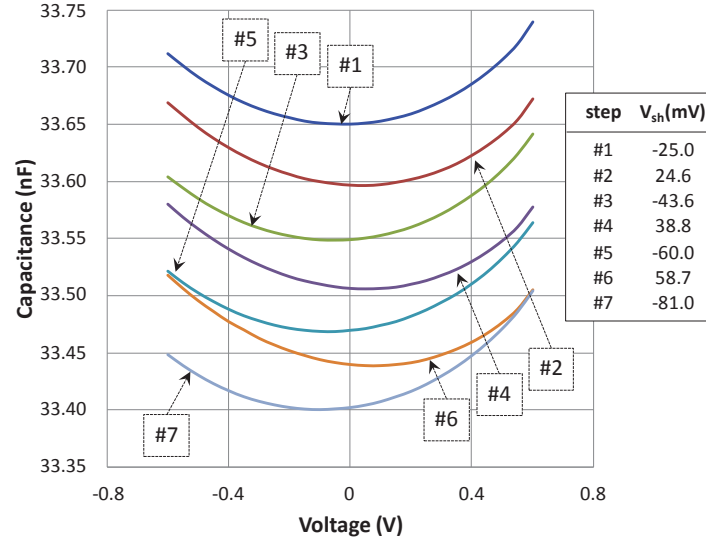


Figure 14: C-V characteristics obtained at the end of each control in the experiment of Figure 13. The table indicates the voltage shifts obtained after each step.